Optimization of spatial resolution and scattering effects for biomedical fluorescence imaging by using sub-regions of the shortwave infrared spectrum

Benjamin Musnier, Maxime Henry, Julien Vollaire, Jean-Luc Coll, Yves Usson, Véronique Josserand, Xavier Le Guével

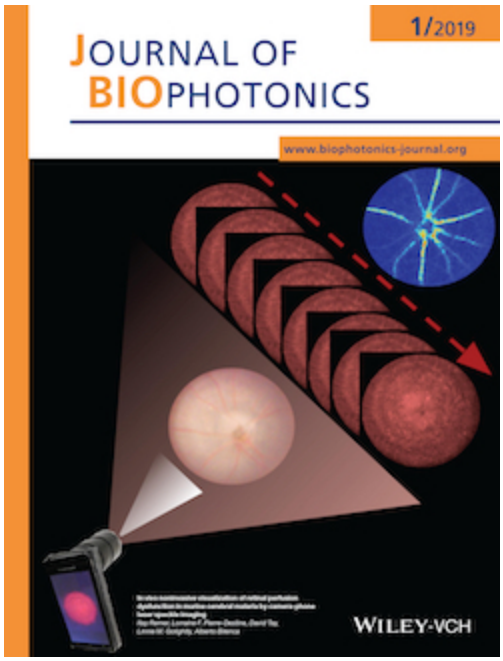

Optimization of spatial resolution and scattering effects for biomedical fluorescence imaging by using sub-regions of shortwave infrared spectrum

Journal:	*Journal of Biophotonics*
Manuscript ID	jbio.202000345.R1
Wiley - Manuscript type:	Full Article
Date Submitted by the Author:	n/a
Complete List of Authors:	Musnier, Benjamin; Institute for Advanced Biosciences, Cancer Targets & Experimental Therapeutics Henry, Maxime; Institute for Advanced Biosciences, Cancer Targets & Experimental Therapeutics Vollaire, Julien; Institute for Advanced Biosciences, Cancer Targets & Experimental Therapeutics Coll, Jean-luc; Institute for Advanced Biosciences, Cancer Targets & Experimental Therapeutics Usson, Yves; TIMC-IMAG Josserand, Veronique; Institute for Advanced Biosciences, Cancer Targets & Experimental Therapeutics Le Guevel, Xavier; Institute for Advanced Biosciences, Cancer Targets & Experimental Therapeutics
Keywords:	shortwave infrared, fluorescence imaging, gold nanoclusters, tissue penetration, scattering

RESPONSE TO REVIEWERS

Reviewer:1

This is an interesting study, in which the influence of PL scattering in tissues is investigated in different SWIR wavelength regions and the authors find that the more of the lower wavelength portion you cut the better the resolution. They exemplify the study by using AuNCs and a commercial IR dye and both phantoms (with actual mouse skin on top) and in vivo imaging of blood vessels in mice in vivo. Focusing on wavelength-dependent scattering is interesting and important and the study provides important information that one needs to take into account when planning and evaluating SWIR imaging experiments. The experiments were well performed and the results are convincing. I was only a bit confused by the presentation of the results. I think it is important to understand and clearly mention at which wavelengths the fluorophores emit (and at which wavelengths they are excited) and which portions of the spectrum are cut away by the LP filters (also for NIR-I that is used for comparison). All that information can be found in the manuscript but it must be put together by the reader themselves (from different Figures and the Methods section). For example, I think it would be good to have one figure that summarizes the spectral and intensity components. Figure 1b should be shown in Figure 2 and also the NIR-I wavelengths (LP filter) should be specified in that Figure (the excitation wavelengths should also be shown in the spectra for example). It would then also be important to mention that each filter cuts off more PL the longer the wavelength. Maybe a zoom into the 1300 to 1500 nm region of the PL spectrum could also be useful because from the current spectrum I do not understand where the PL in the LP1500 images is coming from (and they seem to be the best in Figure 6) because there is no PL in that wavelength region in the spectrum. The study nicely shows that intensity matters (the highest intensity at LP1064 provides the deepest penetration) but if there is sufficient intensity at a given depth, the scattering matters more because the resolution is improved. Maybe the authors can adapt the presentation of their results so they become better accessible. But maybe this is also only my own subjective impression and the other reviewers find the description very clear. In any case, the study is interesting, well suited for the Journal of Biophysics, and the results are convincing and important. Thus, I recommend the publication of this manuscript. Please find a few other comments below.

We thank the reviewers for their critical comments and, as they suggested, we reorganized the Figures 1 and 2 to better illustrate the optical properties of the organic dyes and Au NCs including the set of excitation wavelengths and the sub-SWIR windows obtained with long-pass filters.
We included a zoom of the PL emission spectra for Au NCs using large slits on the spectrometer similar to the LP filter used in our SWIR platform to illustrate that we collect enough PL signal for detection above 1300nm.
We highlight now in the title and through the whole manuscript the critical role of scattering on the spatial resolution in different sub-SWIR windows, which is the key point of this study.

Title: “Improvement of in-depth detection” is not really correct. For going deeper, the LP1064 is best because it provides the highest intensity whereas LP1500 does not show much at deeper regions (Figure S6 shows that very nicely from 1064 to 1300nm). The study is really about wavelength-dependent scattering and I would use the word scattering also in the title.

We thank the reviewer and we agree that scattering should be mentioned in the title. It was replaced in the revised manuscript by:” Optimization of spatial resolution and scattering effects

for biomedical fluorescence imaging by using sub-regions of the shortwave infrared spectrum".

P3, L14: erase or define "extremely bright"

We removed "extremely bright" as it is qualitative observation and quite subjective considering the number of new SWIR emitting contrasts agents with improved brightness published in the literature.

Table 1: Is the LOD not defined as 3 times above the background signal, which means that the SNR should automatically be 3 at the LOD? Error estimations would also be useful for the values in that table.

We totally agree with the reviewer that a limit of detection corresponding to 3 times the signal above background is usually used for analyses in solution and in vitro. We put SNR to 3 in Figure 5b like it was already done in Fig.S1b and in Fig.S3. Error estimations are now included in table 1.

P9, L16: Why "Figure 3"? Should it not be "Figure 5"?

We apologize for this mistake that is now corrected in the revised version.

Figure 5: NIR-I is only shown in 5c. However, it would be important to also compare the intensities (in a and b) of the NIR-I to the SWIR intensities. NIR-I is LP830 (is that one also open until 1700 nm?) and excitation at 780 nm, right? Would one expect any AuNC signal from that setup (the absorption is very low at 780 nm)? Or is NIR-I measured with the dye (but that is supposed to be shown in Figures S2 and S3)? I do not understand the comparison of SWIR and NIR-I in this Figure 5c.

NIR-I emission is determined using a Fluobeam800© instrument with a LED excitation at 780nm (7.8mW/cm^2) and a Si detector that collects photons from 830 to 1000 nm.
Dyes and Au NCs can be excited at 780 nm and emit in the NIR-I and SWIR regions as illustrated more clearly in the new Figure 2. Despite a low absorption of Au NCs above 700nm, they can be detected in mice in the NIR-I (Nanomedicine 20 (2019) 102011) and in the SWIR (Nanoletters 17(10) (2017) 6330-6334) thanks to their broad PL emission in these spectral ranges. While their QY remain moderate in the SWIR (QY<10%), the high sensitivity of the InGaAs sensor and the low background enable their detection at low concentration.
We used the NIR-I window in this article only in the case of the capillary experiment at different depths in intralipids to illustrate the importance of the scattering effect. We did not intend to compare the NIR-I to the SWIR windows in the other experiments since the benefit to move from NIR-I to SWIR/NIR-II in terms of spatial resolution as a function of depth in living tissues has already been well established (Nature Medicine 18(12) (2012) 1841-1846; Proceedings of the National Academy of Sciences 108(22) (2011) 8943…).
As presented in Figure 5c and in Figure S5 the strongest scattering present in the NIR-I region (830-1000nm) as compared to the sub-SWIR windows leads to an important overestimation of the capillary width. Since the sensitivity and the spectral range of the NIR-I or SWIR sensors are different, a direct quantitative comparison of intensity would be unappropriated. Accordingly, we did not include NIR-I data in Figure 5a and 5b.

In order to explain more clearly the comparison between NIR-I and sub-SWIR windows in Figure 5 and S5, we added the following sentence: " In order to quantify the impact of

scattering at different depths on the spatial resolution in the NIR-I region up to 1000 nm and at different SWIR sub-windows, we measured the variation of capillary relative width…"

Reviewer: 2

In this manuscript, the authors evaluated the performance of Au nanoclusters (AuNCs) embedded in a phantom made of PDMS or filled in a capillary tube as emitters in the shortwave infrared region (SWIR). In the focus of their investigation was to quantify the effects of light scattering and spatial resolution in different depth of intralipids. Their results show that choosing only sub-regions of the SWIR spectrum, via long pass filter during the imaging, can significantly improve the spatial resolution and reduce the scattering effect. The gained insights were further proven to be not only relevant for artificial models but also for in vivo imaging of mice.

First of all, this topic is of high interest to the community as SWIR imaging is getting more popular. On the other hand, there is a lack of quantification measures to explain the observed effects in in vivo measurements using an artificial model system. The gap is nicely filled by this manuscript.

To the manuscript. In general, the writing style needs to be improved and checked for grammar errors.

We went through the manuscript and polish the english writing.

The title of the manuscript is not well chosen as the phrase "in-depth" is a synonym for comprehensive or exhaustive, but I think the authors were pointing to the measurements performed in different depths. I would propose to change title to: "Optimization of spatial resolution and scattering effects for biomedical fluorescence imaging by using sub-regions of the shortwave infrared spectrum".

As recommended by the reviewer and also from the first reviewer, we replace the title by the suggested one.

Within the introduction the author wrote that quantum dots were inorganic dyes, which is misleading as the term dye is closely connected to organic dyes. It will be better to write inorganic nanomaterials.

In consequence, we modified inorganic dyes by inorganic materials.

Materials & Methods

- Introduce short-pass (SP) abbreviation
- Figure 1: the letter "a" and "b" are missing
  - Why in Figure 1a is the controller a 808 nm laser?
  - The units for the LED 730 and 830 and nor readable

Results

- Figure 2:
  - Figure 2b please define the y-axis in the manuscript
  - Figure 2c absorbance spectra
    - ♣ The authors show the emission spectra of IRDye800 CW instead of the absorbance spectra!

We performed all the corrections suggested by the reviewers and we apologize for the mistakes regarding the absorbance spectra of IRDye 800 CW.

It will of interest for the reader to show the absorbance and emission spectra of all three contrast agents (ICG, IRDye800CW, and Au NCs) in two plots in the supporting information. In the text the authors wrote that the AuNCs are more than 4 times brighter, which is not supported by the Figure 2b, where only a three times higher intensity was measured. To put this comparison into perspective, the authors should point out that when exciting with the LED 830 nm the dyes only have a very small absorbance in that range. Using the 730 nm LED would have been more interesting as both dyes have a much higher absorbance in that region. As later on the authors work also with the 730 nm LED, I would suggest measuring the detectability of SWIR contrast agents also with this excitation wavelength. The authors should also provide the data or a reference for their statement about the photostability.

We substantially modified the content and the organisation of Figure 1 and Figure 2. Figure 2 now includes absorbance spectra and fluorescence spectra of Au NCs, IRDye 800CW and ICG. We also add a zoom of the optical window between 1300 and 1700 nm to demonstrate the ability to detect PL signal from Au NCs and we illustrate the different set of experiments for better clarity.
Au NCs are in fact 3 times brighter and not 4 times as observed in the Fig.2c. We corrected this mistake within the text. We include in the supporting information the results of an experiment, depicted in the new Fig.S1, confirming the high photostability of Au NCs under LASER exposure (λ= 808nm; 120 mW/cm^2) compared to IRDye 800 CW and ICG.
We agree that an illumination at 730nm matches better the maximum absorption of ICG and IRdye 800 CW and also in the case of Au NCs. However, the power of the LED_{730nm} (16 mW/cm^2) is around 4 times lower than LED_{830nm} (68 mW/cm^2). We found, as shown in Figure S3, that the SNR was better or similar using LED_{830nm} excitation instead of the LED_{730nm} in the capillaries experiment and taking account that longer excitation wavelengths should reach deeper regions of living tissues, we decided to perform experiments with the skin and the mice only at 830nm.

- Figure S1: increase the size of the Figures for a better readability
  - Figure 1 “a” is not shown in the Figure

We improved the readability of Fig.1 and Fig.S1.

The data for higher dye concentrations is missing to show the fluorescence quenching. The authors should also discuss what the reason for the observed quenching could be. As the measurements were performed on droplets, can the drying process lead to increased aggregation at higher dye concentrations and thus influence the photoluminescence (PL) properties? How the LOD in Table 1 was calculated?
We did not observe any quenching of Au NCs up to 4 mg Au/mL which corresponds to 6.6x10^5 nM. Above this concentration, we encountered some toxicity issues in mice and we consider it won’t be biologically relevant to reach such a high concentration in our study.

Indeed, drying process in case of Au NCs would increase the fluorescence (aggregation induced enhancement) so we were very careful to do rapid measurements on the droplets and to avoid drying.
LOD corresponds to the last concentration of samples where the signal-to-noise-ratio is above 3 before it drops. Each measurement has been repeated 3 times. We added the relative errors in the table 1.

In the second point of the results the authors state that their phantom allows to study light scattering with more sensitivity and accuracy. The author should, therefore, mention other established methods and discuss the advantage of their approach.
The author should discuss a bit more in detail, which physical mechanism where influencing the ESF shape and if they would see points of improvement for the phantom.
For a better comparison the authors should also mentioned the thickness of the skin flap and how homogenous it was. This will enable in the later discussion to compare the results of the phantom with skin flap and the capillary measurements.

We used a classical approach that is commonly used over the past 30 years to study *in vivo* events with an artificial model. A homogenous surface can emit SWIR emission over the full range enable to quantify absorption and scattering without interfering with the tissue which is not commonly done by others approach. Indeed, while different theoretical models exists to determine scattering in living tissue such as Rayleigh-Gans-Debye approximation (J. D. Rogers et al., IEEE Journal of Selected Topics in Quantum Electronics, vol. 20, no. 2, pp. 173-186, March-April 2014), the experiments are usually based on the incorporation of particles with controlled size and refractive index within the tissue. Measurements performed with goniometer, or optical tomography followed by imaging analysis can provide very accurate data but incorporating particles suspension homogeneously in living tissues at different depths remain challenging.
Concerning the physical mechanisms, adding the skin on top of the composite only affects diffusion without significant PL signal loss. This indicates scattering to be the main contribution to the ESF shape. We have now included these comments in the manuscript.

Images are obtained with a bright phantom in the optical window considered. The skin was collected on the mouse's back. The thickness of the part collected was between 2 and 3mm. To obtain homogeneous results, different parts of the skin flap were studied. We add a sentence in the discussion to explain the interests of both capillaries and phantom in this study.

In section 3 of the results Figure 5 was meant instead of Figure 3. Furthermore, only in Figure S2 and S3 for the IRDye800 CW an exponential decrease can be observed. For the measurements using the AuNCs the decrease is more or less linear. Interestingly in Figure S3, the IRDye 800CW using a LP1064 nm can be measured up to 6 mm when excited at 830 nm but not for the excitation with 730 nm. What can be the reason, the excitation power density? The authors should also discuss the influence of the excitation wavelengths for the AuNCs at different intralipid layer depths.

We apologize and we corrected this typing mistake in the revised version of the manuscript.
The lack of sensitivity for IRDye 800 CW using LED_{730nm} is partially due to the rather weak power we can use ($16mW/cm^2$) compared to LED_{830nm} ($68\ mW/cm^2$) which explained why we chose the LED in our main set of experiments.

Au NCs have an absorption at 730 nm around 3 times higher than at 830nm while IRDye 800CW has an absorption 10 times higher at 730nm than at 830nm. In case of Au NCs, considering that we used a 4 times more powerful excitation, the obtention of similar results in detection for both excitations in intralipids at different heights (Figure 5b and figure S3a) seem coherent. Surprisingly we were expecting a better sensitivity using LED_{730nm} (Figure S3b) than using LED830nm (Figure 3c) for IRDye 800 CW which was not the case. The reasons could be multiple: 1/ QY of IRDye 800 depending of the wavelength, 2/ influence of scattering and absorption depending of the excitation wavelength. Unfortunately, our platform does not contain the right set of excitation sources to go deeper in this aspect that we believe could be very relevant.

We added the following sentence:" Surprisingly, for IRDye 800CW, we obtained a better sensitivity of detection in intralipids using 830nm excitation instead of 730nm which is quite beyond the maximum of absorption. This effect could be either due to a lower self-reabsorption from the organic dye or a deeper penetration of light at longer wavelength."

- Figure S5: nomenclature of a, b, and c is not correct
  - o For Figure S5a, and b the heights should be added like in Figure S6

We did the corrections in the revised version.

How the authors would explain the strong increase I intensity at 4 mm height for the LP1064 in Figure S6?

The capillary images showed in Figure S6 were not normalized by the exposure time. At 4mm height, a higher exposure time was used. Figure S6 aimed to illustrate the scattering effect of intralipid height in the signal coming from the capillary which clearly appears faster using NIR-I compared to the SWIR spectral window.

The discussion part should be improved given the recommendations given above. Furthermore, a broader perspective should be given how the artificial model measurements can be correlated to the in vivo measurements.

We have now developed the discussion section highlighting the interest of artificial model measurements before to move to *in vivo* measurements as kindly suggested by the reviewer.

Optimization of spatial resolution and scattering effects for biomedical fluorescence imaging by using sub-regions of the shortwave infrared spectrum

*Benjamin Musnier[1], Maxime Henry[1], Julien Vollaire[1], Jean-Luc Coll[*1], Yves Usson[2], Véronique Josserand[1], Xavier Le Guével[1*]*

[1] Cancer Targets & Experimental Therapeutics, Institute for Advanced Biosciences (IAB), University of Grenoble Alpes (UGA)/ INSERM-U1209 / CNRS-UMR 5309 Grenoble, France
[2] TIMC-IMAG, University of Grenoble Alpes, CNRS-UMR 5525, Grenoble, France

E-mail: xavier.le-guevel@univ-grenoble-alpes.fr

Keywords: shortwave infrared, fluorescence imaging, gold nanoclusters, tissue penetration, scattering

Abstract

We evaluated the impact of light-scattering effects on spatial resolution in different SWIR sub-regions by analyzing two SWIR emissive phantoms made of PDMS-gold nanoclusters (Au NCs) composite covered with mice skin, or capillary tubes filled with Au NCs or IRDye 800CW at different depth in intralipids and finally, after administration of the Au NCs intravenously in mice.

Our findings highlighted the benefit of working at the highest tested spectral range of the SWIR region with a 50% enhancement of spatial resolution measured in artificial model when moving from NIR-II (1000- 1300 nm) to NIR-IIa (1300-1450 nm) region, and a 25% reduction of the scattering from the skin determined by point spread function analysis from the NIR-II to NIR-IIb region (1500-1700 nm). We also confirmed that a series of Monte Carlo restoration of images significantly improved the spatial resolution *in vivo* in mice in deep tissues both in the NIR-II and NIR-IIa spectral windows.

Introduction

In vivo fluorescence optical imaging has been widely developed during the last decades in preclinical studies with successful translation toward clinics, in particular for optical guided surgery[1-3]. The visible (400-700 nm) and NIR-I (700-900 nm) optical windows were initially used due to the availability of: i) a large library of commercial or easily synthesizable fluorophores, ii) highly sensitive silicon detectors and, iii) powerful lasers or light emitting diodes (LEDs) available in a wide range of wavelengths. The very high sensitivity of this imaging modality allows molecular imaging with insights of biological features at the cellular level[4]. However, these spectral windows still present severe limitations to achieve both high sensitivity and spatial resolution deep in biological tissues due to the substantial light absorption, high scattering and, autofluorescence of endogenous components[1, 5].

This initiated the search for other spectral windows where these limiting factors would be further reduced. It resulted in considerably improved contrast and spatial resolution, achieved in the shortwave infrared (SWIR) region, also called NIR-II, between 900 and 1700 nm[6]. Since the seminal works of Hongjie Dai's team exploring the SWIR window for biomedical applications in the early 2010's[7-10], major progresses in this new optical window have occurred on three key aspects.

Firstly, the transition from NIR-I to SWIR imaging window has been made possible by the significant advances on indium–gallium–arsenide (InGaAs) camera technology and associated optics. This yielded to affordable detection systems with high sensitivity between 900 nm and 2100 nm and an efficient noise reduction using thermoelectric cooling systems[11].

Secondly, the rapid development of bright SWIR probes made of organic[12] and inorganic materials such as quantum dots[13-15], lanthanide nanoparticles[16, 17], and metal nanoclusters[18-20] has contributed to improve the sensitivity of detection in artificial models and also *in vivo* in small animals. For example, ultra-small gold nanoparticles with diameters smaller than 3 nm, namely gold nanoclusters (Au NCs), have shown relatively high quantum yields with photoluminescence that could be detected above 1250 nm accompanied with a renal clearance when injected in mice[18, 20].

Recently, FDA-approved or at clinical stage contrast agents emitting mainly in the NIR-I and belonging to the cyanine family, like ICG or IRDye 800CW, have been employed for SWIR imaging to envision moving forward to the clinic[21-23] with a first human study reported in 2020[2].

Lastly, imaging processing and reconstruction have been extensively used in most of the biomedical imaging techniques in order to improve image quality and to extract physio-pathological data. For instance, it has been shown that imaging reconstruction based on Monte Carlo restoration of SWIR images could enhance by 59% the spatial resolution and by one order of magnitude the contrast. This enabled to identify non-invasively subtle vascular disorders in bone morphogenetic protein 9 (*Bmp9*)-deficient mice[20].

While SWIR imaging has shown obvious improvement compared to visible and NIR-I optical windows, there is still a lack of studies quantifying the influence of scattering as a function of penetration depth in biological tissues in different SWIR sub-regions.

In this work, we developed and characterized a SWIR imaging system for non-invasive small animal imaging *in vivo* and we investigated the use of two different contrast agents: Au NCs[20] and IRDye 800CW[21] first in artificial models and then *in vivo* in mice.

The first artificial model used to study scattering effects was based on a PDMS/AuNCs composite SWIR emitting bulk covered by a mouse skin flap. The changes observed between the different SWIR sub-regions on scattering point-spread function highlighted a drastic reduction of light scattering at higher wavelengths. This model allowed to obtain robust and complete results with quantitative data, moving one step further to *in vivo* scattering mimicking.

The second artificial model consisted in capillary tubes filled with various concentrations of contrast agents immerged in a 2% intralipid solution, mimicking blood vessels at different depths in strongly scattering tissues. Analyses of these capillary tubes in the NIR-I region and in several SWIR sub-windows, supported the benefit of moving throughout the SWIR window in terms of spatial resolution. Indeed, we show that below 4 mm of intralipid, the higher the fluorescence signal was collected, the more accurately the capillary spatial geometry was reported.

Finally, these findings were validated *in vivo* by imaging a mouse perfused with Au NCs in different SWIR sub-windows, supporting the remarkable improvement in vascular network visualization with enhanced-spatial resolution in depth when collecting a fluorescence signal above 1500 nm and after image processing using a Monte Carlo restoration.

Materials and methods:

Materials. Indocyanine Green (ICG) was purchased from Serb®. IRDye 800CW was purchased from LI-COR Biosciences. Sylgard® 184 Silicone Elastomer was purchased from Neyco S.A. Brand silicone 10 to 1 encapsulants were supplied as two-part liquid component kits. When

liquid components were thoroughly mixed, the mixture cured to a flexible elastomer. Fine bore polythene tubings were purchased from Smiths medical. Emulsion of intralipid 20% which is a lipid emulsion comprising soybean oil was purchased from Merck-France. The intralipid 2% solution was obtained by diluting 10 times the commercial solution in deionized water. All other chemicals and biological reagents were purchased from Merck.

Synthesis of Au NCs. We slightly modified a protocol described by Musnier *et al.*[19] to produce the SWIR-emitted Au NCs using the initial molar ratio Au: Ligand = 1:4. Briefly 250 µL of $HAuCl_4.3H_20$ (20 mM) was added to 4.8 mL water followed by 4 mL of the thiolated ligand mixture mercaptohexanoic acid (MHA, 5 mM)) / tetra(ethyleneglycol)dithiol (TDT, 5 mM) with a volume ratio MHA/TDT= 3 mL/1 mL. The color of the solution changed from yellowish to slightly pale cloudy. After 5 minutes, 250 µL of NaOH (1M) was added dropwise leading to almost colorless sols. After 5 minutes, 150 µL $NaBH_4$ (20 mM in 0.2M NaOH) was introduced dropwise under mild stirring and kept under stirring at 350 rpm for 8 hours. Purification of the Au NCs on 3 kDa cut-off filter column (Amicon) was repeated 3 times to stop the reaction and solutions were kept stored in the fridge until the experiments.

SWIR imaging platform. The imaging system was made of two parts with the excitation and the collection systems as illustrated in **Figure 1a**. The excitation sources consisted of 8 LEDs at 730 nm and 830 nm (4 per wavelength) mounted on a metal ring (Opto) at 30 cm working distance. Each LED was coupled to a ground glass, acting as a homogenizer, a collimator (Opto) and a set of shortpass (SP) filters (SP 750 nm, SP 850nm (Thorlabs), SP 1150 nm (Edmund Optics)) extinguishing unwanted parasite wavelengths. The LED_{730nm} excitation yielded a beam with an irradiance of 16 mW/cm^2 on a 30 cm^2 area and the LED_{830nm} excitation yielded a beam with an irradiance of 68 mW/cm^2 on a 23 cm^2 area (**Figure 1b**). Photons were collected through a set of long-pass (LP) filters (LP Colored 850 nm (Thorlabs)) and LP1064 nm (Semrock)) followed by interchangeable long pass filters (Thorlabs) delineating four SWIR imaging sub-regions (1064 nm-1700 nm for LP1064 nm; 1250 nm-1700 nm for LP1250 nm; 1300 nm-1700 nm for LP1300 nm; 1500 nm-1700 nm for LP1500 nm) (**Figure 2d**).

The filtered light was focused on an InGaAs camera chip (NIRvana 640ST, 640 x 512 array, 900 nm to 1700 nm (Princeton)) using fixed focal length lenses (Navitar) of 25 mm (Field of view (FOV): 114 mm x 91 mm) or 50 mm (FOV: 43mm x 34 mm). The InGaAs camera was cooled to -60 °C, the analog to digital (AD) conversion rate was set to 2 MHz to have the highest image quality, the gain was set to "high", and different exposure times were selected to reach

about 50% of the dynamic range of the camera (0-46000 gray levels). All SWIR images were background corrected using LightField imaging software® (Princeton).

NIR-I imaging. Experiments were performed with a NIR 2D-Fluorescence reflectance-imaging device (Fluobeam 800®, Fluoptics, France). The excitation was provided by a class 1 expanded laser source at 780 nm and the irradiance on the imaging field was 10 mW/cm^2. A CCD camera (696 x 576 array, 300 to 1000 nm, FOV: 127 mm x 95 mm) collected the fluorescence signal through a long pass filter (LP830 nm).

Contrast agents' fluorescence detectability. Drops of contrast agents (10 µL in PBS 10mM) at different concentrations were imaged through the 50 mm fixed focal length lens under 830 nm excitation source using adapted exposure times. The concentration linearity range (R^2 > 0.995) and the limit of detection (SNR > 3) on the 1064 nm–1700 nm region were determined for Au NCs and IRDye 800CW.

Composite Au NCs / PDMS artificial model. A mixture of the two liquids from Sylgard® 184 Silicone Elastomer component kit was poured in a homemade Fortal mold consisting of a small tank with a pillar inside. After air bubbles removing using a water pump, the mold was placed overnight in an oven (60°C). The PDMS bulk presented then a small tank with a volume of 1cm^3 where the contrast agent was embedded. This photoluminescent part was made of a mix of Au NCs lyophilized powder (90 mg), silicone elastomer (1 g) and curing agent (100 mg). After air bubbles removing using a water pump, the mold was placed overnight in an oven (60°C). After complete drying, the bulk edges were cut to reach a square of 2 cm by 2 cm and the top surface was homogenized using a Leica CM3050 S cryostat to remove surface irregularities. The composite bulk, apart from an emitting window of 5 mm by 5 mm on the top surface, was covered with black foil (Thorlabs) to avoid reflections and parasite scattering.
The composite Au NCs / PDMS bulk was imaged under the 830 nm excitation with the 25 mm fixed focal length lens before and after superposition of a skin flap taken from a BALB/c nude mouse (Janvier labs, France) as illustrated in **Figure 4a**. A set of 3 images was taken for each condition to perform robust and reproducible analysis.

Edge and point spread function data analysis. Multi-line cross-sectional intensity profile analysis of the emitting bulk was performed using ImageJ software. The profiles obtained also called edge spread functions (ESF) were then extracted to perform data treatment and analysis

through the software GNU Octave. A script was used to normalize these ESF before deriving them by calculating the difference between two adjacent values. The gathered functions, known as empirical point spread functions (empirical-PSF), were fitted by Gaussian functions to obtain fitted point spread functions (fitted-PSF). After normalization of the fitted PSF, the full width at half maximum (FWHM) was extracted using Origin Pro 7 software (Origin©) in order to compare the influence of SWIR sub-windows on scattering. In our study, ESF and PSF were used only to assess light-scattering that is much greater than the theoretical diffraction scattering of our lens (< 1 pixel).

Capillaries imaging. Effect of scattering on the spatial resolution was estimated using a fine bore polythene tubing (OD = 0.96 mm / ID = 0.58 mm; Portex) filled with Au NCs or IRDye 800CW and immersed in a 2% Intralipid[24, 25] solution (**Figure 1c**) at increasing depths between 1 and 8 mm.

Each condition was recorded through the 50 mm fixed focal length lens. The two contrast agents were excited at 730 nm and 830 nm for SWIR imaging (exposure time from 100ms to 2s) and at 780 nm for NIR-I imaging (exposure time from 150ms to 1s). Measurements were reproduced 3 times for each condition to perform robust and reproducible analyses.

Data analysis. Images analysis was performed using ImageJ software. Measurements of signal intensity were done in a define region of interest (ROI) manually located on the capillary without intralipid and kept unchanged for all intralipid heights. The noise was measured at the edge of images in an area without relevant signal. Signal to noise ratio (SNR) was calculated as the mean signal intensity from the capillary divided by the noise. An arbitrary threshold value of 3 was fixed as a limit for SNR. Below this value, we considered that the signal from the capillary was not significant.

To evaluate scattering effect on each image, a cross-sectional intensity profile of the capillary was performed using the plot profile module of imageJ software. The full width at half maximum (FWHM) evaluated by a fit of a Gaussian curve (Origin Pro 7 software) was obtained on each profile to describe the capillary width imaged by the camera for each condition. The FWHM or relative width obtained was compared with the real width of the capillary as a percentage defined as:

$$eq\ 1 : \% = fit\ FWHM{-}constructor\ width * 100.$$

***In vivo* mouse experiment.** A six weeks old NMRI nude female mouse (Janvier Labs, France) was anesthetized (air/isoflurane 4%) and a catheter (BD neoflon) was positioned in the tail vein. The femoral artery was then incised to let the blood flow out and Au NCs contrast agent (360 µM in PBS 1X) was perfused intravenously via the catheter. Exagon (1 mL/kg) was injected immediately after to sacrifice the mouse. Imaging was performed immediately after the sacrifice using the 830 nm excitation and the 50 mm fixed focal length lens.

Results

1- Fluorescence detectability of SWIR contrast agents

Contrast agents emitting in the visible or NIR-I optical windows have been widely studied and characterized in the last decades, using well known and affordable silicon based detectors and spectrometers[26, 27]. SWIR-emitting contrast agents still remain poorly evaluated due to the short list of candidates as well as the rarity of *in vivo* SWIR imaging systems in research laboratories. In order to develop *in vivo* imaging followed by medical applications in the SWIR, recent works reported the ability to use cyanine dyes ICG and IRDye 800CW as SWIR contrast agents[2, 22, 28]. Despite moderate quantum yields (QY) in this optical window with photoluminescence (PL) from the tail of their emission spectra, these probes presented the advantage to be already clinically approved, thus being references for comparison of new SWIR contrast agents.

While ICG and IRDye 800CW offered similar absorbance profiles with a maximum at 775 nm in PBS buffer, Au NCs showed two NIR absorbance bands at 680 nm and 775 nm accompanied by a tail up to 1000 nm (**Figure 2a**). Au NCs exhibited a broader PL emission in the SWIR at longer wavelengths than IRDye 800CW and ICG as depicted in **Figures 2b and 2d**.

In this study we selected Au NCs and the cyanine dye IRDye 800CW as reference probe instead of ICG. In fact, by measuring the PL emission of a droplet and normalizing to the exposure time, we found IRDye 800CW 7 folds brighter in the SWIR than ICG at the same concentration in PBS (**Figure 2c**). Furthermore, IRDye 800CW presents the advantages of a high colloidal stability, a fast renal clearance[21, 28], and the ability to be conjugated to molecules of interest. Au NCs' PL was found more than 4 times higher than IRDye 800 CW'PL at the same concentration (**Figure 2c**), with the ability to excite them over a wide window of wavelengths (from 400 to 850nm) (**Figure 2d**) and a much higher photostability under NIR-I light exposure at 140 mW/cm^2 during 2 hours (**Figure S1**).

We first determined the sensitivity of detection of the two contrast agents (Au NCs and IRDye 800CW) in the SWIR (1064 nm-1700 nm) by measuring their PL at different concentrations. For IRDye 800 CW, the linear range of detection was estimated between 98 nM and 25 µM. Above 25 µM, fluorescence quenching occurred in both NIR-I and SWIR optical windows. For Au NCs, the signal was linear between 22 nM and 90 µM without any quenching at the highest concentration measured. At similar SNR ~5.5, the sensitivity of detection of Au NCs was 4 times better than for IRDye 800CW (89 nM and 391 nM respectively) (**Figure S2b, Table 1**).

Contrast agents	Limit of detection (LOD)	SNR at LOD
Au NCs	22±2 nM	4.43±0.22
IRDye 800CW	98±5 nM	3.05±0.15

Table 1. Sensitivity of detection in SWIR of Au NCs and IRDye 800CW solutions.

2- Optical scattering studies on phantom covered by a mouse skin flap in different SWIR sub-windows

A SWIR calibration tool was developed by mixing an elastomer and lyophilized Au NCs powder on a PDMS container. The composite bulk obtained presented a strong PL even at low exposure times on a large and homogeneous emitting area over the full SWIR range (50% of saturated signal at 50 ms exposure time using LP1500 nm). This highly PL emitting and precisely designed phantom allowed to study light scattering due to the skin with more sensitivity and accuracy. Thus, a skin flap with thickness between 2 to 3mm collected from a mouse's back was placed over the calibration tool as illustrated in **Figure 3a**. Scattering induced by the skin was studied in different SWIR sub-regions by measuring the changes on edge and point spread function (ESF and PSF).

Multi-line cross-sectional intensity profile analyses were performed on the side of the emitting bulk. By following the approach summarized in **Figure 3b**, it was possible to obtain FWHM of PSF for each SWIR sub-windows. In theory, a perfectly straight edge would lead, for the bulk without skin on top, to a rectangular function for ESF and thus a FWHM tending toward zero. Our bulk wasn't a perfectly straight-line and orthogonal block leading to the ESF shapes observed without skin.

The comparison of the normalized PSF Gaussian functions for the bulk covered or not by skin, as showed in **Figure 4a**, allowed to directly evaluate the impact of scattering from the skin. As

depicted in **Figure 4a**, the differences observed between the images obtained using different LPs indicated a decrease of diffuse scattering at longer wavelengths from a blurry image with LP1064 nm to a sharp one with LP1500 nm.

The FWHM of each normalized PSF Gaussian function was extracted to characterize the impact of scattering from the skin for the different LPs (**Figure 4b**). For instance, for the LP 1064 nm, we observed a FWHM of 4.7 pixels (pixel size: 70 µm * 70 µm) with skin versus 2.2 pixels (+113%) without skin. A relative comparison of results for the different SWIR LPs documents the important decrease of the FWHMs obtained with skin (- 25%, - 13% and - 8% for LP1250 nm, LP1300 nm and LP1500 nm compared to LP1064 nm) as well as a diminution of the differences between FHMW with and without skin (72%, 67% and 44% for LP1250 nm, LP1300 nm and LP1500 nm). The FWHM for the emitting bulk with skin decreased when using higher imaging wavelengths, highlighting a reduction of diffuse scattering and collection of more realistic images.

3- Wavelength collection range influences light scattering and impacts in-depth spatial resolution.

We present here the results obtained with Au NCs at the 830 nm excitation (**Figure 5**). Measurements performed under excitation at 730 nm and with IRDye 800CW are available in the supporting information (Figures S3, S4). Notably, for IRDye 800CW, we obtained a better sensitivity of detection in intralipids using 830 nm excitation instead of 730 nm which was quite beyond the maximum of absorption. This effect could be either due to a lower self-reabsorption from the organic dye or a deeper penetration of light at longer wavelength.

As a first observation, when increasing the depth, the PL signal decreased exponentially regardless of the wavelength collection band used as illustrated (**Figures 5a, S3).** To evaluate the impact of depth and wavelength collection on spatial resolution, a capillary tube was filled with Au NCs (45.5 µM in PBS 10 mM) and immersed at various depths in Intralipid 2%. This standard protocol is used to mimic a contrast agent circulating in a blood vessel within biological tissue *in vivo* since Intralipid 2% has been shown to display similar optical properties (µa and µs') than the human skin[29].

We considered the maximum penetration depth when SNR was > 3. Au NCs could be then detected down to 8 mm, 7 mm and 5 mm using LP1064 nm, LP1250 nm and LP1300 nm respectively (**Figure 5b**). With the LP1500 nm, the PL intensity from Au NCs in the capillary was too weak to be detected deeper than 1 mm, which was expected considering the low concentration and the PL profile of this contrast agent with signal dropping after 1400 nm.!

In order to quantify the impact of scattering at different depths on the spatial resolution in the NIR-I region up to 1000 nm and at different SWIR sub-windows, we measured the variation of capillary relative width (see **Figure S5** for FWHM variations) compared to its real size (coefficient detailed in eq.1 was calculated for each condition). As illustrated in **Figure 5c**, the relative width linearly increased with depth when collecting signal in the NIR-I region. At 1 mm depth, the capillary relative width was already overestimated 5 times (2.91 mm ± 0.09 mm compared to the constructor capillary width of 0.58 mm) and this distortion highly increased with depth, leading to a blurry and undefined capillary image (9.10 mm ± 0.27 mm corresponding to a distortion to the constructor capillary width of 1569% ± 47%) at a depth of 4 mm (**Figures 5c, S6**).

In contrast, in the SWIR spectral window, no significant variation of capillary relative width was detected up to 2 mm depth, regardless of the LP used, with 103% ± 0.5%; 99% ± 0.7% and 98% ± 0.3% for LP1064 nm, LP1250 nm and LP1300 nm respectively. Above 3 mm depth, using LP1064nm, the relative width started to raise exponentially from 123% ± 1.3% at 3 mm to 1599% ± 3.4% at 7 mm. Interestingly, by selecting higher wavelength collection ranges, we noticed a reduced variation of the capillary's relative width (137% ± 7.8% and 170% ± 14.9% at 4 mm depth for LP1250 nm and LP1300 nm respectively) compared to the LP1064 nm. However, it appeared that above 4 mm even selecting sub-regions at longer wavelengths, scattering became very elevated, and led to an overestimation of the width of the capillary (**Figures 5c, S5-S7**).

4- *In vivo* vascular imaging using different SWIR sub-windows

To further investigate the influence of scattering on the empirical resolution *in vivo* in live animals, we took whole body SWIR images of a nude mouse after it received an intravenous perfusion of Au NCs in the tail vein.

The images obtained from the different SWIR sub-regions (**Figures 6a, S8-S10**) showed an obvious improvement of spatial resolution when moving towards to longer wavelengths were selected as compared to classical NIR-I imaging.

Using LP1064 nm, we observed a diffuse signal from the skin that tended to blur vessels contrast. For LP1300 nm and even more for LP1500 nm, a large number of blood vessels of heterogeneous sizes and at different depths could be detected thanks to the reduced scattering and decreasing skin auto-fluorescence. A cross-sectional profile was made through a vessels rich area to appreciate both vessels contrast and resolution using different LPs (**Figure 6a**). Although Au NCs PL decreased at the highest wavelengths, a large improvement in terms of

signal-to-noise and signal-to-skin ratios as well as spatial resolution was observed as illustrated by higher and sharper pic corresponding to blood vessels.

We then used a Monte Carlo restoration processing with an additional high pass filtering (MCR+HP filter)[20] on the previous images. As seen in **Figure 6b**, the contrast was significantly improved after processing. The comparison of the plot profiles after application of the MCR+HP filter showed narrower widths of the blood vessels, getting closer to the real sizes especially when using the LP1064 nm and LP1300 nm (**Figures 6b, S8-10**).

Discussions and conclusion

The SWIR spectral range (900-1700 nm) has recently emerged as a promising bioimaging window for non-invasive and real-time monitoring of biological processes thanks to a strong reduction of light scattering and absorption by blood and biological tissues *in vivo* resulting in significant improvement of sensitivity and spatial resolution in depth[1]. Recent studies using contrast agents such as ICG [21, 28] and IRdye800CW[28] initially designed for NIR-I imaging and commonly administered to human patients yielded dramatically augmented performances when used in SWIR imaging.

Besides, new contrast agents with high PL in the SWIR have been investigated in small animals. Among these, SWIR-emitting probes based on ultra-small gold particles (<3 nm) called Au NCs showed a high colloidal stability over several months in water and buffer solutions, exhibit high PL at wavelength above 1250 nm[18], thus making these SWIR emitters promising contrast agents. Preclinical studies in mice showed no toxicity, a good circulation time (blood half-life: $t_{1/2\alpha}$~ 0.43 h) with low nonspecific accumulation in organs and efficient renal elimination. These Au NCs have been used in *in vivo* in mice and allowed noninvasive detection of vascular disorders in bone morphogenetic protein 9 (*Bmp9*)-deficient mice[20].

In this work, we used Au NCs to investigate the impact of light scattering on the empirical spatial resolution in different SWIR sub-regions on different artificial models and in mice. Using a bright SWIR emissive composite bulk made of Au NCs and PDMS with sharp edges, we explored the scattering effects of the skin which has been identified as the main contribution to the distortion of the edge's geometry. Compare to others artificial models based on the inclusion of particles with known sizes, absorption and refractive index in medium or in tissues[30], this artificial model did not modify the sample, and in our case, the integrity of the living tissue.

We measured an overestimation of the FWHM by 113% in the presence of skin when using LP1064 nm, and a drastic reduction at higher SWIR wavelengths with a FWHM decreased by 25% between LP1064 nm and LP1500 nm. This quantitative study confirms the interest to explore NIR-IIb as the most suitable SWIR sub-region for the non-invasive exploration of living tissues. We also confirmed a decrease of scattering at longer wavelengths with a more accurate conservation of the real size of capillary immerged in a scattering medium at different depths. Indeed, we showed that below 4 mm of intralipid, the capillary width was almost half less overestimated using the LP1250 nm (137%) or LP1300 nm (170%) than with the LP1064 nm (292%).

This trend was confirmed *in vivo*. The enhancement obtained by imaging in the 1500 – 1700 nm SWIR sub-region led to a better detection in depth, with sharper and more realistic cross-sectional profiles of the blood vessels.

In complement of the improvement that could be brought by selecting appropriate contrast agents and detection wavelengths, a major importance should be given to image treatment and restoration as a powerful tool to reduce scattering and improve biological resolution. **Figure 6b (**see also **Figures S8-10)** show an example of contrast enhancement and spatial resolution improvement obtained with Monte Carlo restorations.

Custom-made microfluidic chips will be also highly relevant artificial models mimicking heterogeneous blood vessels in their natural environment and in the presence of blood-flow. They provide suitable systems with channels covering all the spectra of the mice vascular network, from micro-capillaries to larger vessels and provide dual information on spatial and temporal resolution.

With a NIR-IIb being an optimum SWIR sub-region, safer and brighter contrast agents in this optical window are urgently needed to demonstrate the clear breakthrough of SWIR imaging compared to NIR-I for clinical applications.

In conclusion, we showed the significant reduction of scattering from endogenous tissues at longer wavelengths in the SWIR window, using two artificial models and in small animal. Our results highlighted the necessity to develop contrast agents with strong brightness in the last and most promising SWIR window (1500-1700 nm) also called NIR-IIb. The combination of long wavelengths SWIR imaging, imaging processing and restoration allows moving non-invasive optical imaging one-step forward toward the generation of powerful tools for optical imaging adapted to the clinical practice.

Acknowledgements

We would like to thank Cancéropôle Lyon Auvergne Rhône-Alpes (CLARA), ITMO Cancer Aviesan program "Equipment" of Plan Cancer III (2017), Plan Cancer (C18038CS), and the Foundation ARC (R17157CC) for their financial support. The Optimal imaging platform is supported by France Life Imaging (French program "Investissement d'Avenir" grant; "Infrastructure d'avenir en Biologie Santé", ANR-11-INBS-0006) and the IBISA French consortium "Infrastructures en Biologie Santé et Agronomie".

References

1. G. Hong, A. Antaris and H. Dai, *Nature biomedical engineering*, 2017, **1**, 0010 (0011-0022).
2. Z. Hu, C. Fang, B. Li, Z. Zhang, C. Cao, M. Cai, S. Su, X. Sun, X. Shi, C. Li, T. Zhou, Y. Zhang, C. Chi, P. He, X. Xia, Y. Chen, S. S. Gambhir, Z. Cheng and J. Tian, *Nature Biomedical Engineering*, 2020, **4**, 259-271.
3. B. Kahramangil and E. Berber, *Journal of Surgical Oncology*, 2017, **115**, 848-855.
4. M. Koch, P. Symvoulidis and V. Ntziachristos, *Nature Photonics*, 2018, **12**, 505-515.
5. J. Zhao, D. Zhong and S. Zhou, *Journal of Materials Chemistry B*, 2018, **6**, 349-365.
6. L.-Y. Huang, S. Zhu, R. Cui and M. Zhang, *Analytical Chemistry*, 2020, **92**, 535-542.
7. G. Hong, S. Diao, J. Chang, A. L. Antaris, C. Chen, B. Zhang, S. Zhao, D. N. Atochin, P. L. Huang, K. I. Andreasson, C. J. Kuo and H. Dai, *Nature Photonics*, 2014, **8**, 723-730.
8. Y. Zhang, Y. Zhang, G. Hong, W. He, K. Zhou, K. Yang, F. Li, G. Chen, Z. Liu, H. Dai and Q. Wang, *Biomaterials*, 2013, **34**, 3639-3646.
9. J. T. Robinson, G. Hong, Y. Liang, B. Zhang, O. K. Yaghi and H. Dai, *Journal of the American Chemical Society*, 2012, **134**, 10664-10669.
10. G. Hong, J. C. Lee, J. T. Robinson, U. Raaz, L. Xie, N. F. Huang, J. P. Cooke and H. Dai, *Nature Medicine*, 2012, **18**, 1841-1846.
11. S. S. Kang, D.-M. Geum, K. Kwak, J.-H. Kang, C.-H. Shim, H. Hyun, S. H. Kim, W. J. Choi, S.-H. Choi, M.-C. Park and J. D. Song, *Scientific Reports*, 2019, **9**, 12875.
12. Q. Yang, Z. Ma, H. Wang, B. Zhou, S. Zhu, Y. Zhong, J. Wang, H. Wan, A. Antaris, R. Ma, X. Zhang, J. Yang, X. Zhang, H. Sun, W. Liu, Y. Liang and H. Dai, *Advanced Materials*, 2017, **29**, 1605497.
13. M. Zhang, J. Yue, R. Cui, Z. Ma, H. Wan, F. Wang, S. Zhu, Y. Zhou, Y. Kuang, Y. Zhong, D.-W. Pang and H. Dai, *Proceedings of the National Academy of Sciences*, 2018, **115**, 6590.
14. Y. Zhang, G. Hong, Y. Zhang, G. Chen, F. Li, H. Dai and Q. Wang, *ACS Nano*, 2012, **6**, 3695-3702.
15. D. Franke, D. K. Harris, O. Chen, O. T. Bruns, J. A. Carr, M. W. B. Wilson and M. G. Bawendi, *Nature Communications*, 2016, **7**, 12749.
16. D. J. Naczynski, M. C. Tan, M. Zevon, B. Wall, J. Kohl, A. Kulesa, S. Chen, C. M. Roth, R. E. Riman and P. V. Moghe, *Nature Communications*, 2013, **4**, 2199.
17. S. Ding, L. Lu, Y. Fan and F. Zhang, *Journal of Rare Earths*, 2020, DOI: https://doi.org/10.1016/j.jre.2020.01.021.

18. Y. Chen, D. Montana, H. Wei, J. Cordero, M. Schneider, X. Le Guevel, O. Chen, O. Bruns and M. Bawendi, *Nanoletters*, 2017, **17**, 6330-6334.
19. B. Musnier, K. D. Wegner, C. Comby-Zerbino, V. Trouillet, M. Jourdan, I. Hausler, R. Antoine, J. L. Coll, U. Resch-Genger and X. Le Guevel, *Nanoscale*, 2019, **11**, 12092-12096.
20. Z. Yu, B. Musnier, K. D. Wegner, M. Henry, B. Chovelon, A. Desroches-Castan, A. Fertin, U. Resch-Genger, S. Bailly, J.-L. Coll, Y. Usson, v. josserand and X. Le Guével, *ACS Nano*, 2020, **14**, 4973-4981.
21. J. A. Carr, D. Franke, J. R. Caram, C. F. Perkinson, M. Saif, V. Askoxylakis, M. Datta, D. Fukumura, R. K. Jain, M. G. Bawendi and O. T. Bruns, *Proceedings of the National Academy of Sciences of the United States of America*, 2018, **115**, 4465-4470.
22. S. Zhu, Z. Hu, R. Tian, B. C. Yung, Q. Yang, S. Zhao, D. O. Kiesewetter, G. Niu, H. Sun, A. L. Antaris and X. Chen, *Advanced Materials*, 2018, **30**, 1802546.
23. S. Zhu, B. C. Yung, S. Chandra, G. Niu, A. L. Antaris and X. Chen, *Theranostics*, 2018, **8**, 4141-4151.
24. K. Welsher, S. P. Sherlock and H. Dai, *Proceedings of the National Academy of Sciences*, 2011, **108**, 8943.
25. S. Ali and B. Wesam, *Polish Journal of Medical Physics and Engineering*, 2017, **23**, 121-126.
26. R. R. Zhang, A. B. Schroeder, J. J. Grudzinski, E. L. Rosenthal, J. M. Warram, A. N. Pinchuk, K. W. Eliceiri, J. S. Kuo and J. P. Weichert, *Nature Reviews Clinical Oncology*, 2017, **14**, 347-364.
27. J.-B. Li, H.-W. Liu, T. Fu, R. Wang, X.-B. Zhang and W. Tan, *Trends in Chemistry*, 2019, **1**, 224-234.
28. Z. Starosolski, R. Bhavane, K. B. Ghaghada, S. A. Vasudevan, A. Kaay and A. Annapragada, *PLOS ONE*, 2017, **12**, e0187563.
29. L. T. Tamara and N. T. Suresh, *Journal of Biomedical Optics*, 2001, **6**, 167-176.
30. J. D. Rogers, A. J. Radosevich, J. Yi and V. Backman, *IEEE Journal of Selected Topics in Quantum Electronics*, 2014, **20**, 173-186.

a

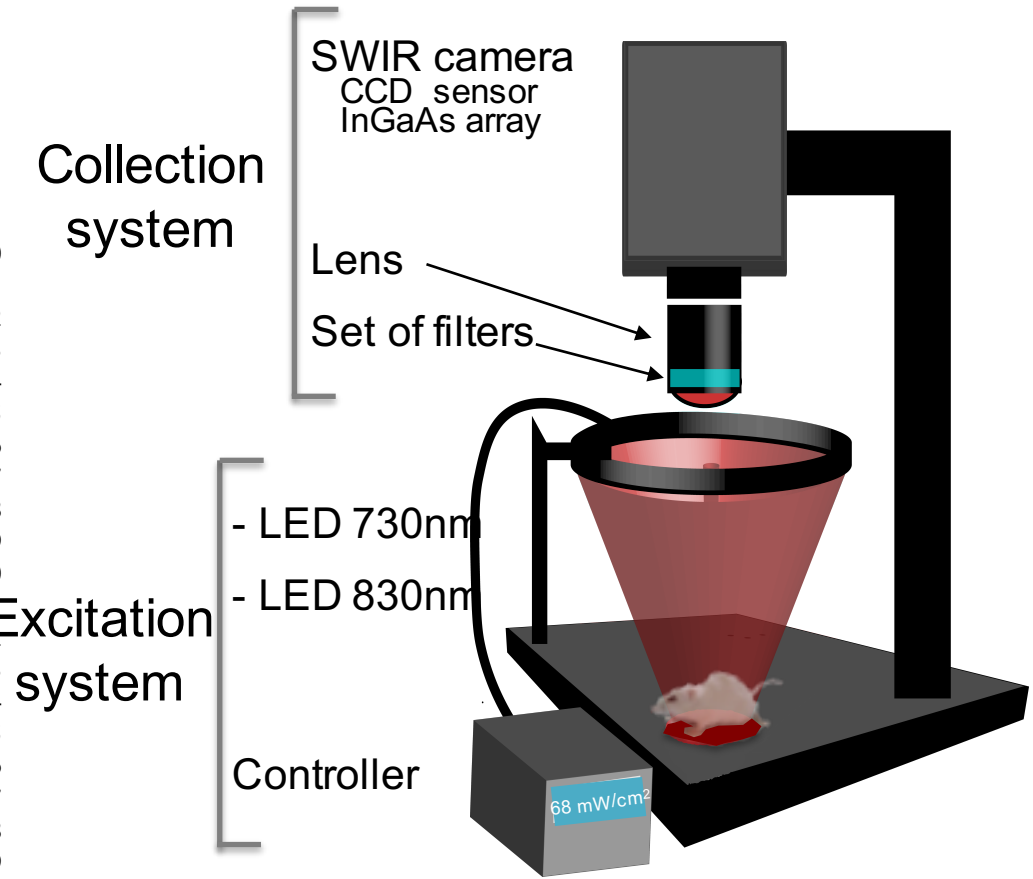

b

Excitation source	λ= 730 nm	λ= 830 nm
Power density (mW/cm^2)	16	68
Irradiation area (cm^2)	30	23

c

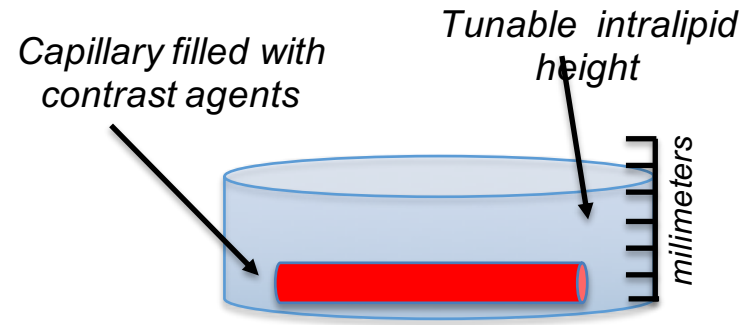

Figure 1. (a) Schematic side views of imaging setup for artificial and *in vivo* models. (b) Excitation source setting. (c) Schematic view of the artificial model using capillary tubes immersed on high scattering intralipid medium.

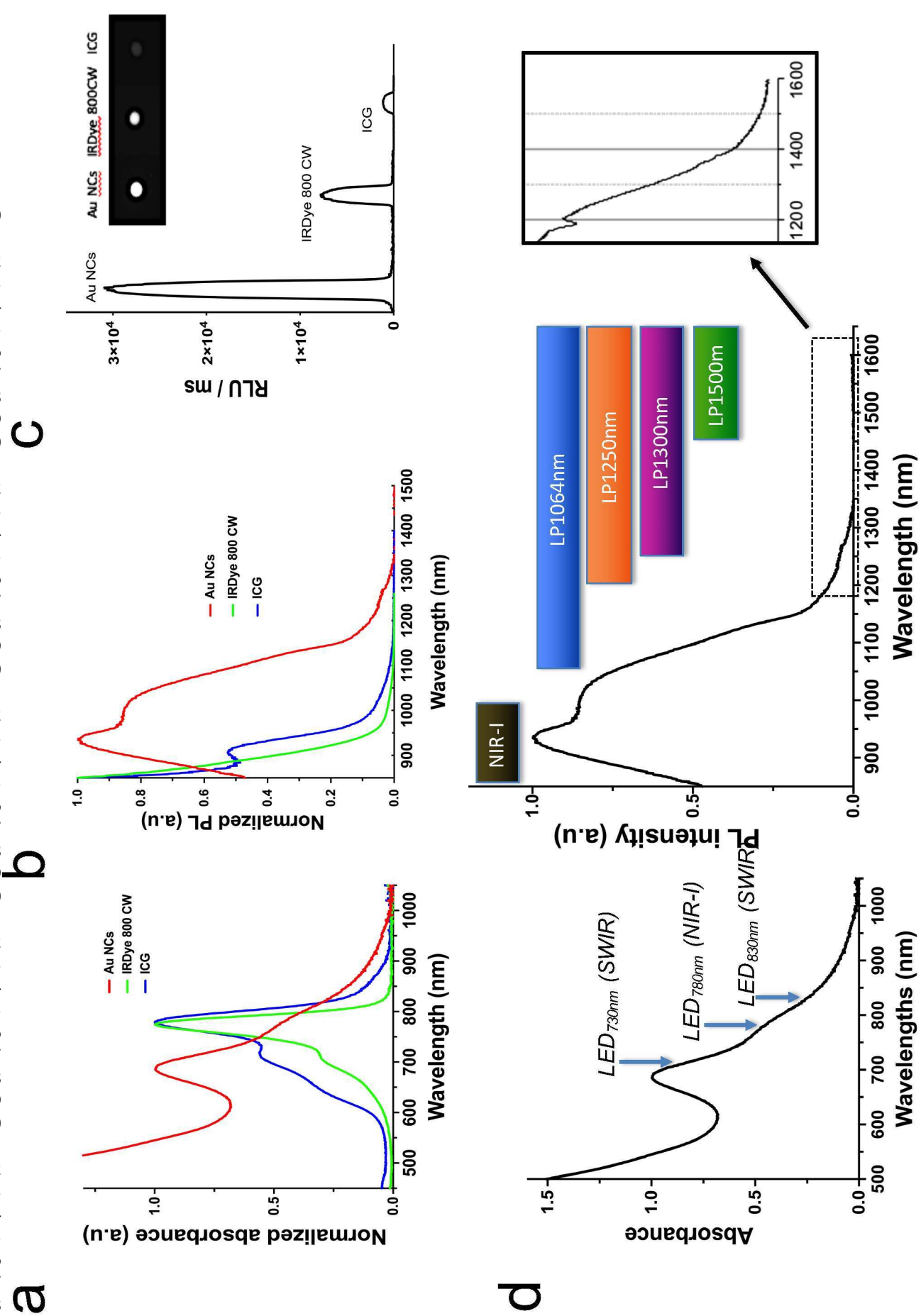

Figure 2. (a) Normalized absorption (λ= 685 nm for Au NCs and λ= 775 nm for IRDye 800CW and ICG) and (b) normalized PL emission (λ= 937 nm for Au NCs and λ= 850 nm for IRDye 800CW and ICG) spectra of Au NCs , IRDye 800CW and ICG diluted in PBS (10mM). (c) Image and intensity cross-sectional profile of contrast agents (drops of Au NCs, IRDye 800CW and ICG) at 50 nM using LP1064 nm. (d) Set up on the excitation wavelengths and emission windows for NIR-I and SWIR experiments (Au NCs absorption and emission profile).

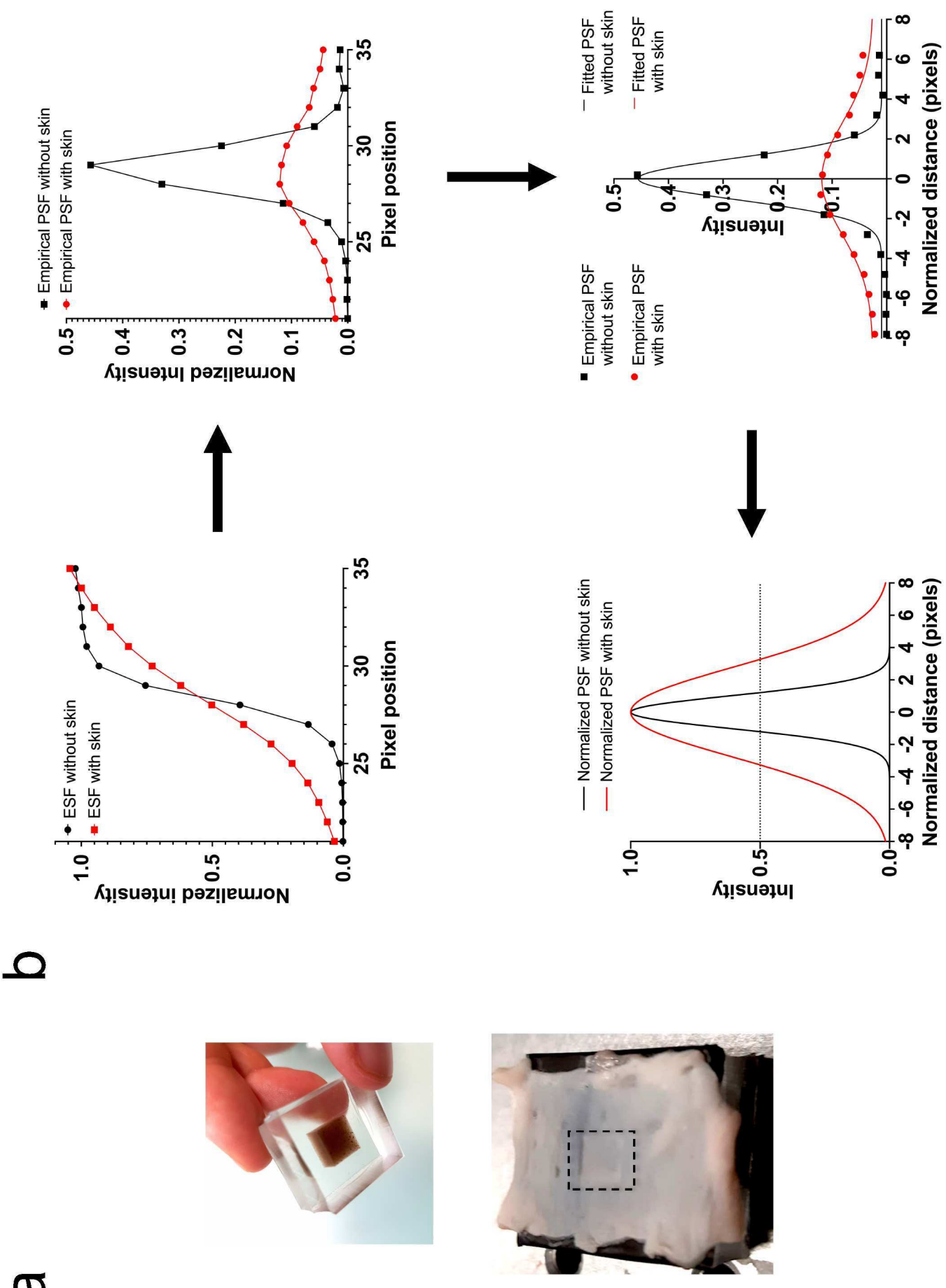

Figure 3. (a). Au NCs/PDMS composite with skin flab from BALB/c nude mice. (b). Steps for scattering normalized PSF determination using the composite Au NCs / PDMS artificial model.

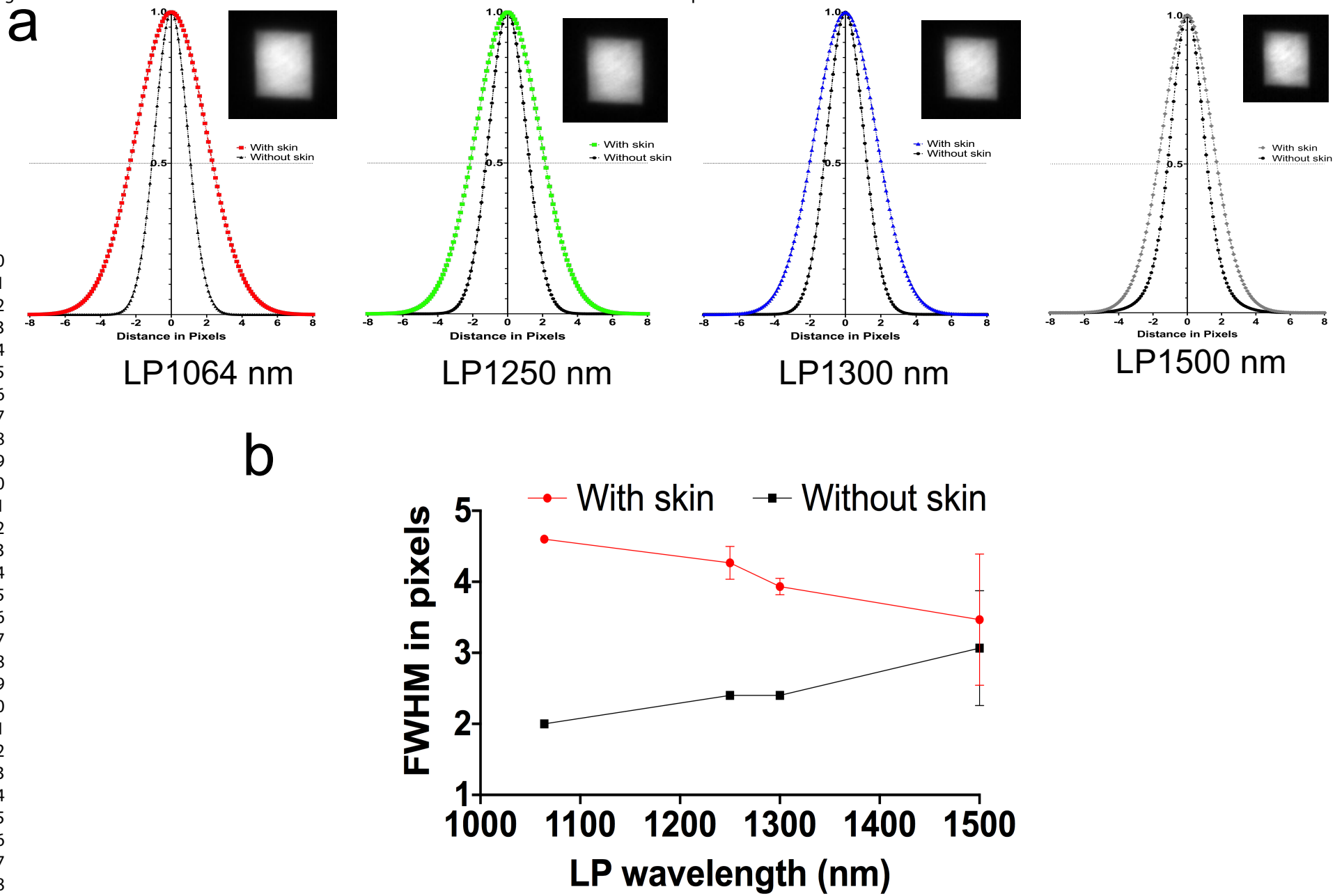

Figure 4. (a) Normalized PSF and images of Composite PDMS / Au NCs artificial model covered by skin using different SWIR LPs. (b) FWHM of Normalized PSF of Composite Au NCs / PMDS artificial model covered and unvovered by mouse skin using different SWIR sub-windows.

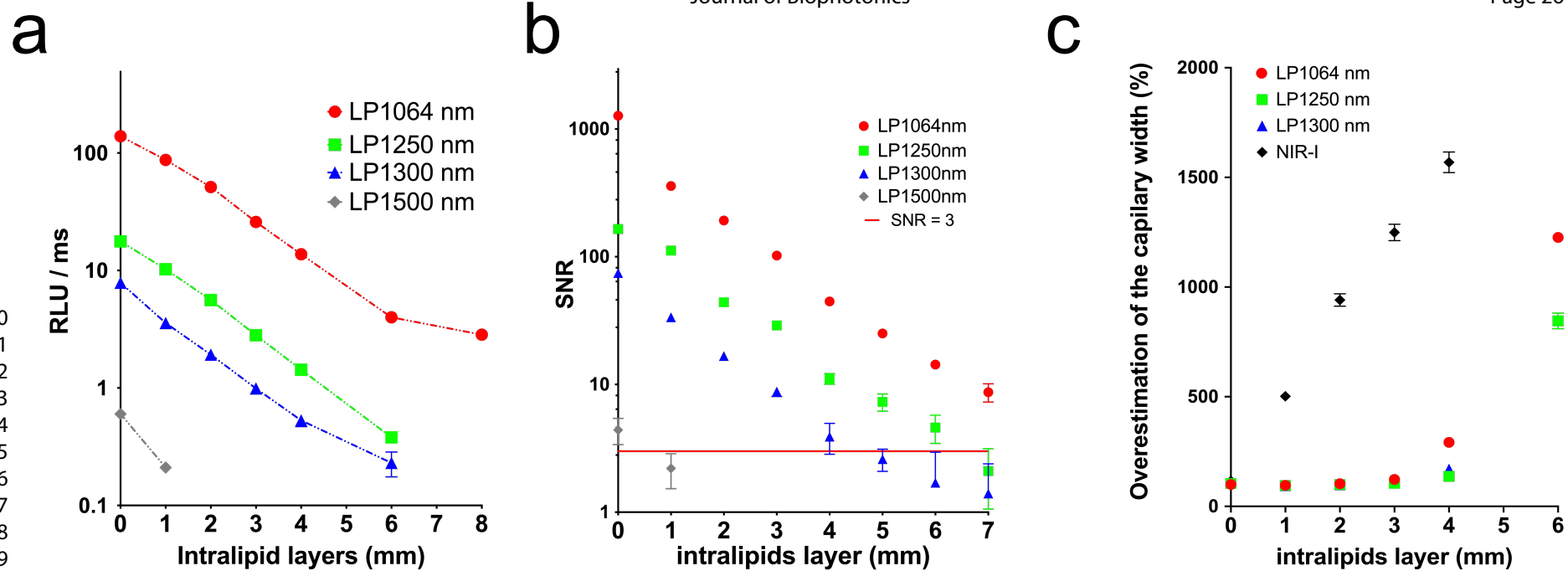

Figure 5. (a) Logarithmic scale intensity profiles under different intralipid height using different SWIR LPs for Au NCs. $\lambda_{exc.}$ 830 nm. (b) Logarithmic representation of Signal to Noise Ratio of Au NCs contrast agent using different SWIR LPs as a function of the intralipid height and (c) Comparison between FWHM of cross-sectional profiles in capillary images and constructor capillary's width in different SWIR sub windows and for NIR-I.

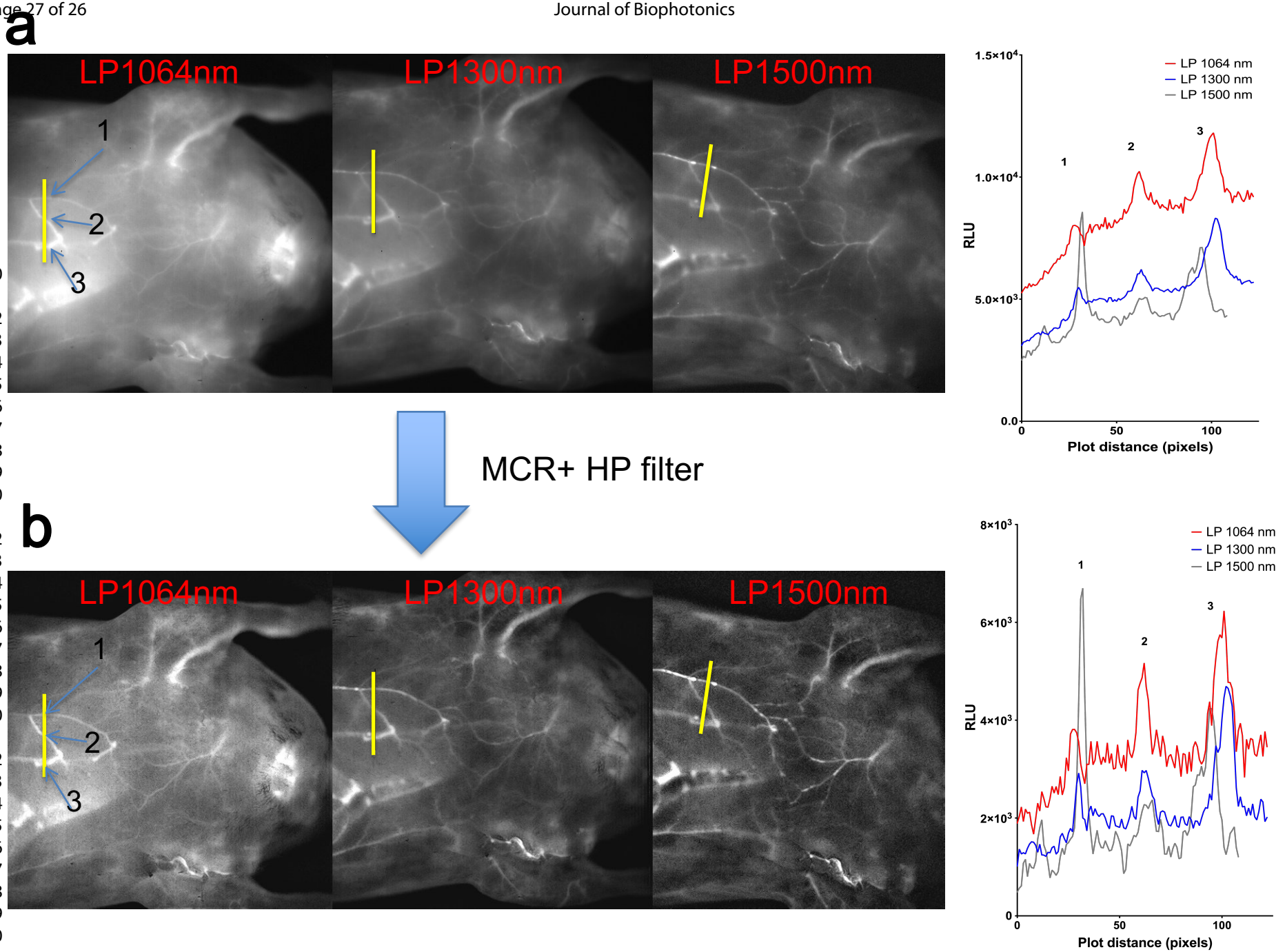

Figure 6. *In vivo* vascular imaging and cross-sectional plot profiles of ventral blood vessels after i.v. injection of Au NCs using LP1064 nm, LP1300 nm, LP1500 nm (a) before and (b) after Monte Carlo constrained restoration with an additional filtering (MCR+HP filter).